Slab lenses from simple anisotropic media

Thomas Dumelow,[1,2,3,*] José Alzamir Pereira da Costa,[1] and Valder Nogueira Freire[2]
[1]*Departamento de Física, Universidade Federal do Rio Grande do Norte, 59072-970 Natal RN, Brazil*
[2]*Departamento de Física, Universidade Federal do Ceará, Campus Pici, 60455-900 Fortaleza CE, Brazil*
[3]*Departamento de Física, Universidade do Estado do Rio Grande do Norte, Costa e Silva, 59625-620 Mossoró RN, Brazil*[†]
(Received 18 December 2004; revised manuscript received 14 October 2005; published 19 December 2005)

Slab lenses formed from nonmagnetic anisotropic media are described. In the case of a uniaxial medium, the requirement is $\epsilon_{xx}>0, \epsilon_{zz}<0$, z being the uniaxis direction, normal to the front and back optical surfaces of the lens. The properties of the lenses are similar to those of lenses made from a negative index medium. However, they only function in p polarization and the image is not free of aberrations. An example of a suitable medium, applicable to far-infrared frequencies, is a crystal of triglycine sulfate.

DOI: 10.1103/PhysRevB.72.235115 PACS number(s): 78.20.Ci, 42.15.−i, 42.79.Bh

I. INTRODUCTION

One of the most exciting prospects associated with the recent surge in interest in negative refractive index materials is the possibility of slab lenses, first proposed by Veselago in 1968.[1] Both sides of a lens of this type would be flat and parallel to each other, yet an object on one side of the lens would project a real image on the other side. Pendry[2] predicted that such a lens could, in fact, act as a so-called "superlens," producing images smaller than the traditional diffraction limit would allow. The type of material originally suggested by Veselago had both the dielectric function ϵ and magnetic permeability μ negative (double negative medium). In the special case of $\epsilon=-1$ and $\mu=-1$, perfect reconstruction of the source field should be possible. Artificial structures using split-ring resonators[3,4] have been proposed to give negative effective ϵ and μ values, and negative refraction has been confirmed experimentally in such structures in the microwave region.[5,6] Alternative artificial photonic crystals have also been shown to exhibit negative refraction.[7–15]

The lensing properties of slabs of both of these types of materials have been convincingly demonstrated,[16–19] and some promising advances, including subwavelength imaging, have been made. Despite these successes, a perfect lens of the type described by Pendry[3] would require the use of a material with very exacting properties.[20,21] Practical achievement of such properties represents a considerable challenge. Nevertheless, a much simpler slab lens, although far from satisfying perfect lens criteria, may be conceivable. This paper describes such a lens made from a simple anisotropic medium. Although focusing is restricted to p-polarized radiation and the image is not free of aberrations, the type of imaging described by Veselago[1] should indeed be possible.

II. NEGATIVE REFRACTION IN UNIAXIAL DIELECTRIC MEDIA

The optics that can lead to negative refraction in a uniaxial dielectric medium was described in previous papers.[22,23] Here we define a light ray to undergo negative refraction when, on passing through an interface, the incident and refracted ray lie on the same side of the surface normal. Such behavior can of course occur trivially if none of the principal axes lies along this normal, but the present paper is not concerned with such cases, as they do not, in general, lead to the type of lensing properties described in here.

Consider radiation passing through an interface in the geometry shown in Fig. 1(a). Layer 1 is a vacuum layer and layer 2 is a uniaxial nonmagnetic medium whose uniaxis lies along z, normal to the interface. The in-plane wave-vector component k_x is then given by

$$k_x = k_0 \sin\theta_i, \tag{1}$$

where $k_0=\omega/c$ and θ_i is the angle of incidence. Boundary conditions dictate that this k_x value holds both sides of the interface.

Maxwell's equations may be applied in the two layers to find the z components of the wave vector. In the first (vacuum) layer, this gives

$$k_{1z}^2 = k_0^2 - k_x^2. \tag{2}$$

In the second layer, however, it is necessary to differentiate between the behavior of the s-polarized waves (**E** field along

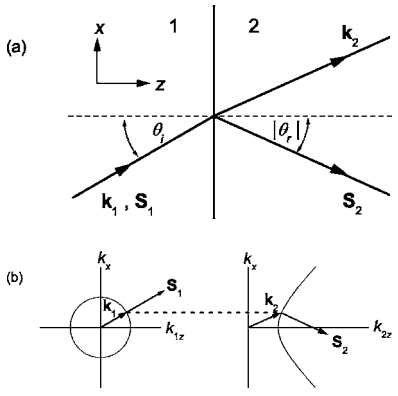

FIG. 1. (a) Directions of wave vectors and Poynting vectors for p-polarization refraction at an interface between air and a uniaxial medium with $\epsilon_{xx}=1$, $\epsilon_{zz}=-1$ for $\theta_i=30°$. (b) Equal frequency contours on each side of the interface for a single frequency value (for simplicity, the negative k_{2z} curve is not shown). The value of k_x for $\theta_i=30°$ is shown as a dashed line joining the two contours.

y, perpendicular to the plane of incidence formed by the wave vector $\mathbf{k}$ and the surface normal) and p-polarized waves ($\mathbf{H}$ field along y).[24] The former are commonly referred to as ordinary waves and the latter as extraordinary waves. The two solutions are, for s polarization,

$$k_{2z}^2 = k_0^2 \epsilon_{xx} - k_x^2, \tag{3}$$

and for p polarization,

$$k_{2z}^2 = k_0^2 \epsilon_{xx} - k_x^2 \frac{\epsilon_{xx}}{\epsilon_{zz}}, \tag{4}$$

where ϵ_{xx} and ϵ_{zz} represent the principal components of the dielectric function of the uniaxial medium.

It is important to choose the correct root for k_{1z} and k_{2z}. In order to do this, we look at the power flow $\mathbf{S}$, which, for the incident and refracted rays considered here, must be from left to right in both media (i.e., S_{1z} and S_{2z} are both positive). In the first medium (vacuum), the power flow is parallel to the wave vector, and we choose the positive root for k_{1z}. In order to determine the correct root for k_{2z}, we represent the power flow by the Poynting vector $\mathbf{S}=\mathbf{E}\times\mathbf{H}^*$ and determine the time-averaged value $\langle\mathbf{S}\rangle = 1/2\ \mathrm{Re}(\mathbf{S})$. For s polarization, this gives, in terms of the $\mathbf{E}$ field in layer 2,

$$\langle \mathbf{S}_2 \rangle = \frac{1}{2}\mathrm{Re}\left(\frac{k_x^*}{\mu_0 \omega}|E_y|^2, 0, \frac{k_{2z}^*}{\mu_0 \omega}|E_y|^2 \right). \tag{5}$$

For p polarization, the equivalent expression in terms of the $\mathbf{H}$ field is

$$\langle \mathbf{S}_2 \rangle = \frac{1}{2}\mathrm{Re}\left(\frac{k_x}{\epsilon_0 \omega \epsilon_{zz}}|H_y|^2, 0, \frac{k_{2z}}{\epsilon_0 \omega \epsilon_{xx}}|H_y|^2 \right). \tag{6}$$

The power flow in s polarization is parallel to the real part of the wave vector, just as in vacuum, and $\mathrm{Re}(k_{2z})$ is always positive (or zero). In p polarization, the power flow direction (or angle of refraction θ_r) is given by

$$\tan\theta_r = \frac{\langle S_{2x}\rangle}{\langle S_{2z}\rangle} = \frac{\mathrm{Re}(k_x/\epsilon_{zz})}{\mathrm{Re}(k_{2z}/\epsilon_{xx})}. \tag{7}$$

For simplicity, let us consider for the moment only propagating waves with no absorption, in which case $\epsilon_{xx}, \epsilon_{zz}$, and k_{2z} are all real [k_x is automatically real from Eq. (1)]. Since S_{2z} must be positive, Eq. (6) shows that the sign of k_{2z} must be the same as that of ϵ_{xx}. The case of interest in this communication is ϵ_{xx} positive and ϵ_{zz} negative, in which case k_{2z} is always real and positive (other combinations of signs of ϵ_{xx} and ϵ_{zz} are considered in the earlier papers[22,23]). Equation (7) shows that, for k_x positive (positive angle of incidence θ_i), the angle of refraction θ_r will then be negative, indicating negative refraction as shown in the example in Fig. 1(a).

The above behavior may be represented pictorially using equal frequency contours[9,15] (referred to as equifrequency surfaces in the three-dimensional case) in the k_x-k_z plane. At any given frequency, Eqs. (2) and (4) give the allowed wave vectors for propagating waves, yielding the contours shown in Fig. 1(b). Thus Eq. (2) is represented by a circle of radius k_0 and Eq. (4) by two hyperbolas[25,26]—one for positive k_{2z} values and the other [not shown in Fig. 1(b)] for negative k_{2z} values. Power flow is always perpendicular to these contours. The resulting Poynting vector directions are then the same as those shown in Fig. 1(a). Note that there is always an acute angle between $\mathbf{S}_2$ and $\mathbf{k}_2$, so the anisotropic medium is classed as a forward wave material,[23] and the refracting mechanism is thus similar to that which occurs in the type of photonic crystals studied by Luo *et al.*[9] or Hu and Chan.[27] The relevant equal frequency contours in the latter case are circles centered around the crystal M point, and negative refraction, at least for small k_x, occurs in much the same way as shown in Fig. 1(b). This contrasts with isotropic double negative materials, which have $\mathbf{S}$ and $\mathbf{k}$ antiparallel, and are thus backward wave media.

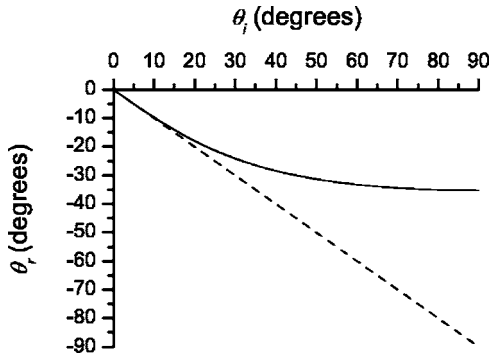

FIG. 2. Angle of refraction as a function of angle of incidence at the interface between air and a medium with $\epsilon_{xx}=1$, $\epsilon_{zz}=-1$. The solid line shows the angle of refraction calculated using Eq. (7) and the dashed line gives the result of using a paraxial approximation represented by Eq. (9).

The solid line in Fig. 2 shows θ_r, calculated from Eq. (7), as a function of θ_i for the case $\epsilon_{xx}=1$, $\epsilon_{zz}=-1$. It is instructive to compare these results with Snell's law, which, for refraction from vacuum into an isotropic medium, gives $\sin\theta_i/\sin\theta_r = n$, where n represents the refractive index of the refracting medium. In the present case, we find the relationship between $\sin\theta_i$ and $\sin\theta_r$ by combining Eqs. (1), (4), and (7). In the absence of absorption, this gives

$$\sin^2\theta_r = \frac{\epsilon_{xx}\sin^2\theta_i}{\epsilon_{zz}^2 + \sin^2\theta_i(\epsilon_{xx} - \epsilon_{zz})}. \tag{8}$$

There is therefore not, in general, a linear relationship between $\sin\theta_i$ and $\sin\theta_r$ as would be expected for isotropic media. Nevertheless, in the small angle (paraxial) limit $\sin^2\theta_i \ll 1$, Eq. (8) reduces to

$$\frac{\sin^2\theta_i}{\sin^2\theta_r} = \frac{\epsilon_{zz}^2}{\epsilon_{xx}}, \tag{9}$$

and Snell's law is obeyed with an effective refractive index n_{eff} equal to

$$n_{\mathrm{eff}} = \frac{\epsilon_{zz}}{\epsilon_{xx}^{1/2}}. \tag{10}$$

In the special case of $\epsilon_{xx}=1$, $\epsilon_{zz}=-1$, this gives $n_{\mathrm{eff}}=-1$, so that $\theta_r=-\theta_i$. This is represented by the dashed line in Fig. 2. Despite the large discrepancies at high angles, the paraxial

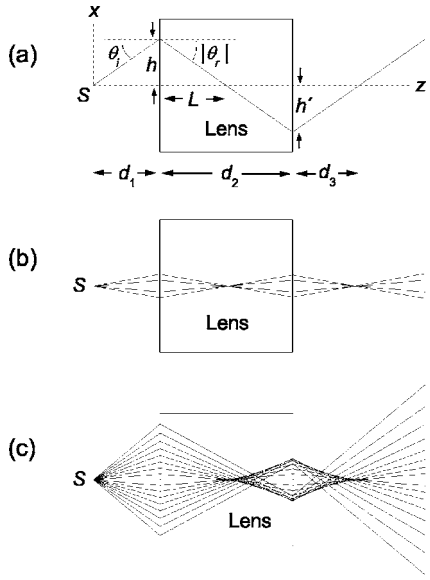

FIG. 3. (a) Path of a single ray from a source S passing through a slab of thickness d_2. (b) Focusing of radiation from source S by a slab lens with $\epsilon_{xx}=1$, $\epsilon_{zz}=-1$ within the range of incident angles $-10° \leqslant \theta_i \leqslant 10°$. (c) Focusing of radiation from source S by a slab lens with $\epsilon_{xx}=1$, $\epsilon_{zz}=-1$ within the range of incident angles $-40° \leqslant \theta_i \leqslant 40°$. In both (b) and (c), the slab is placed at a position such that $d_2=2d_1$.

approximation holds good to within 3% at incident angles of 10° or less.

The fact that light is not only reflected negatively, but also obeys Snell's law, albeit in the small-angle limit, suggests that the plane interface described above should have interesting lensing properties, and that a slab lens of the type described by Veselago[1] is worth investigating.

III. IMAGE FORMATION IN THE PARAXIAL LIMIT

We now consider the use of a material with $\epsilon_{xx}>0, \epsilon_{zz}<0$ as a slab lens. For simplicity, we first consider the situation in which the paraxial approximation discussed above holds true. The geometry used is that shown in Fig. 3. A point source S is positioned at $x=0$, $z=0$. The left-hand face of a slab of material, of thickness d_2, is positioned at $z=d_1$. In p polarization, a ray emanating from S refracts negatively at the $z=d_1$ interface as shown in Fig. 3(a), and, assuming the slab is sufficiently thick, crosses the z axis at a distance L from this interface, within the slab. The ray is once again refracted negatively at the other side of the slab, crossing the z axis at a distance d_3 to the right of the slab.

At the first interface, Snell's law gives, in the paraxial approximation,

$$n_{\text{eff}} = \frac{\theta_i}{\theta_r} = \frac{h/d_1}{-h/L} = -\frac{L}{d_1}. \tag{11}$$

Similarly, at the second interface,

$$n_{\text{eff}} = \frac{h'/d_3}{-h'/(d_2-L)} = -\frac{d_2-L}{d_3}. \tag{12}$$

Eliminating L from these two equations, we get

$$d_1 + \frac{d_2}{n_{\text{eff}}} + d_3 = 0. \tag{13}$$

Thus, in the paraxial approximation, the point at which rays cross the z axis to the right of the lens does not depend on the initial angle of incidence, so the rays are focused to a single point at $z=d_1+d_2+d_3$. Note, however, that a physical solution (d_3 positive) to Eq. (13) only exists if $d_2 \geqslant |n_{\text{eff}}|d_1$. This is a reflection of the fact that if the slab is not sufficiently thick, there is neither an internal nor an external focus.

A simple ray diagram showing the formation of an image from a slab with $\epsilon_{xx}=1$, $\epsilon_{zz}=-1$, corresponding to $n_{\text{eff}}=-1$, is shown in Fig. 3(b) for incident angles up to 10°. The ray directions used in drawing this diagram were calculated from Eq. (7). As expected from Eq. (13), an image is formed at the position at which $d_1+d_3=d_2$. This is also the condition for image formation by a slab lens of isotropic material with $\epsilon=-1$ and $\mu=-1$, corresponding to a true refractive index $n=\sqrt{\epsilon}\sqrt{\mu}=-1$, as considered by Veselago[1] and Pendry.[2] In fact, Eq. (13) gives the image position, in the paraxial limit, for a slab lens of any isotropic double negative medium if n_{eff} is replaced by the true refractive index. In the case of such a medium with $\epsilon=-1$ and $\mu=-1$, the equation is not restricted to the paraxial limit, and holds for all incident angles. Furthermore, in this special case the amplitudes of the evanescent waves corresponding to $|k_x|>k_0$ are also restored at the image position, leading, in principle, to a perfect reconstruction of the image.[2]

To go beyond the use of geometrical optics in modeling image formation, we consider the refocusing of a Gaussian beam, for which the paraxial approximation should be valid for a normally incident beam provided the beam waist is not too narrow. The procedure necessary for the analysis has been detailed by Kong *et al.*[28] The beam waist takes the place of the source S, and is centered at $x=0$, $z=0$. In the absence of the slab medium, the resulting magnetic field at any xz coordinate can be represented, providing $z>0$, as

$$H_y = \int_{-\infty}^{\infty} \psi(k_x) e^{i(k_x x + k_{1z} z)} dk_x, \tag{14}$$

where

$$\psi(k_x) = -\frac{g}{2\sqrt{\pi}} e^{-g^2(k_x - k_0 \sin\theta)^2/4}. \tag{15}$$

$2g$ represents the beam width at its waist and θ represents the effective incident angle of the overall beam. The changes required for $z<0$ are trivial.

In the presence of the slab, the fields in each of the three layers n can be represented as

$$H_{ny} = \int_{-\infty}^{\infty} [a_n(k_x) e^{ik_{nz}z} + b_n(k_x) e^{-ik_{nz}z}] e^{ik_x x} dk_x. \tag{16}$$

The coefficients a_n are for radiation propagating in the direction of increasing z and the coefficients b_n are for radiation propagating in the direction of decreasing z. Thus one can see by inspection that $a_1=\psi(k_x)$ and that $b_3=0$. The other coefficients may be calculated taking into account the mul-

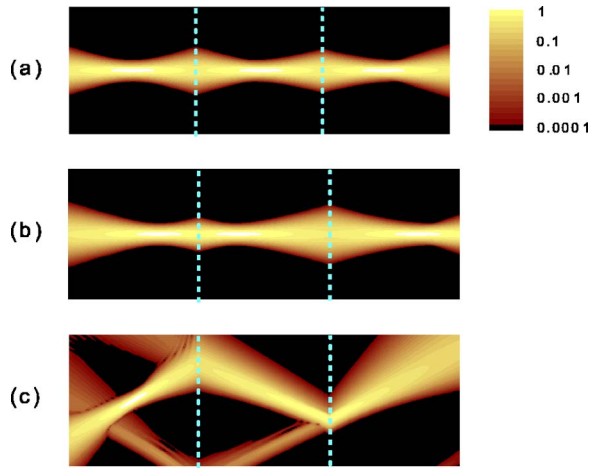

FIG. 4. (Color online) Refocusing of a Gaussian beam by a slab lens. The vertical dashed lines represent the faces of the slab. The material parameters are $\epsilon_{xx}=1$, $\epsilon_{zz}=-1$, the slab thickness is $d_2=50\lambda$, and the beam width is characterized by $g=2\lambda$. (a) $d_1=25\lambda$, $\theta=0$; (b) $d_1=10\lambda$, $\theta=0$; (c) $d_1=25\lambda$, $\theta=30°$. In each case, the power density scale is in arbitrary units. Note that some values fall outside the range of the scale shown. These values are represented as either black (low power density) or white (high power density).

tiple reflections and transmissions involved (see Kong *et al.*[28] for details), where the single interface reflection and transmission coefficients, for incidence from vacuum to the uniaxial medium, are given by,[22] respectively,

$$r=\frac{\epsilon_{xx}k_{1z}-k_{2z}}{\epsilon_{xx}k_{1z}+k_{2z}}, \tag{17}$$

$$t=\frac{2\epsilon_{xx}k_{1z}}{\epsilon_{xx}k_{1z}+k_{2z}}. \tag{18}$$

The values of the **E** fields are obtained by integrating the two terms in Eq. (16) separately, and applying $\nabla\times\mathbf{H}=-i\omega\mathbf{D}$ to each result. The power density can then be determined at any xz coordinate from the Poynting vector, calculated from the values of the **H** and **E** fields.[28]

The results of numerical calculations, based on the above analysis, for a p-polarized Gaussian beam incident on a slab lens with $\epsilon_{xx}=1$, $\epsilon_{zz}=-1$ are shown in Fig. 4. We use $g=2\lambda$, where λ represents the free-space wavelength, corresponding to a half-angle beam divergence of 9°. Figure 4(a) shows the result at normal incidence when $d_1=d_2/2$. At $\theta_i=9°$, the paraxial approximation results in an error of only 2.5% in θ_r, so it appears reasonable to compare the image position with that expected from the $d_1+d_3=d_2$ rule that paraxial theory predicts in the present case. We take the image position to be that where the intensity, to the right of the lens, is a maximum. Using this criterion, we find $d_1+d_3=48.4\lambda=0.964d_2$, very close to the prediction of paraxial theory. In Fig. 4(b), we check the effect of moving the incident beam waist closer to the lens, which should move the image away from the lens by an equal amount. This is actually what we find, and once again $d_1+d_3=48.4\lambda$.

Despite the promising nature of the above results, some care should be taken in their interpretation. In particular, we have taken the radiation to be p-polarized, and considered a two-dimensional representation of a Gaussian beam. In effect this amounts to a beam, polarized with its **H** field along y, focused to a waist that is not circular but is in the form of a line directed along y. In the case of a Gaussian beam focused to a circular spot, one would normally expect half the "normal incidence" radiation to be p-polarized and half to be s-polarized (even in the presence of a polarizer). The s-polarized radiation would not be refocused and, in the case of $\epsilon_{xx}=1$, would continue to diverge as if the lens were not there. Thus half the radiation would not be refocused.

The oblique incidence result is shown in Fig. 4(c). Here, the refocusing is not so good, but negative refraction itself is distinctly visible, along with the effect of internal and external reflections. Note, however, that although the reflected rays show up clearly on the log scale used in the figure, the actual reflectivities are of order 10^{-2}. In this case, paraxial theory clearly cannot be applied. Image formation away from the paraxial limit is considered in the following section.

IV. IMAGE FORMATION AWAY FROM THE PARAXIAL LIMIT

There are clearly very few practical situations in which the paraxial approximation will give a good model of image formation for this type of lens. Figure 2 shows that deviations from this model become large for angles of incidence much greater than used in the previous section. Figure 3(c) is a ray diagram showing image formation by a slab with $\epsilon_{xx}=1$, $\epsilon_{zz}=-1$ for the range of incident angles $-40°\leqslant\theta_i\leqslant 40°$. For this wider range of angles, there is still a clear focusing effect, as in Fig. 3(b), but there are now significant aberrations. The envelope of the rays forms a caustic curve similar to that caused by spherical aberrations in more conventional lens systems,[29] and the effective image is now closer to the lens than paraxial theory would predict.

In order to model a source radiating in all directions in the xy plane, we consider S as an oscillating line current source. For the present case, applicable to p polarization, we consider this to be a source of magnetic current K directed along the y axis at $x=0$, $z=0$. The analysis is essentially the same as that used for the Gaussian beam in the previous section, but with $\psi(k_x)$ replaced by[30]

$$\psi(k_x)=-\frac{\omega\epsilon_0 K}{4\pi k_{1z}}. \tag{19}$$

Note that the lateral width (along x) of the slab is implicitly assumed to be infinite. Focusing by a slab of finite width will therefore be slightly different from the idealized calculations shown here.

Figure 5 shows focusing from a line source by a slab with $\epsilon_{xx}=1$, $\epsilon_{zz}=-1+0.0001i$ (a small amount of absorption has been included to help stabilize the integral when the source is close to the slab). Figure 5(a) shows the time-averaged power flow when $d_1=10\lambda$, $d_2=20\lambda$. Here $d_1, d_2\gg\lambda$, so we expect the lens to behave according to the predictions of geometrical optics, and the focusing effect is indeed essen-

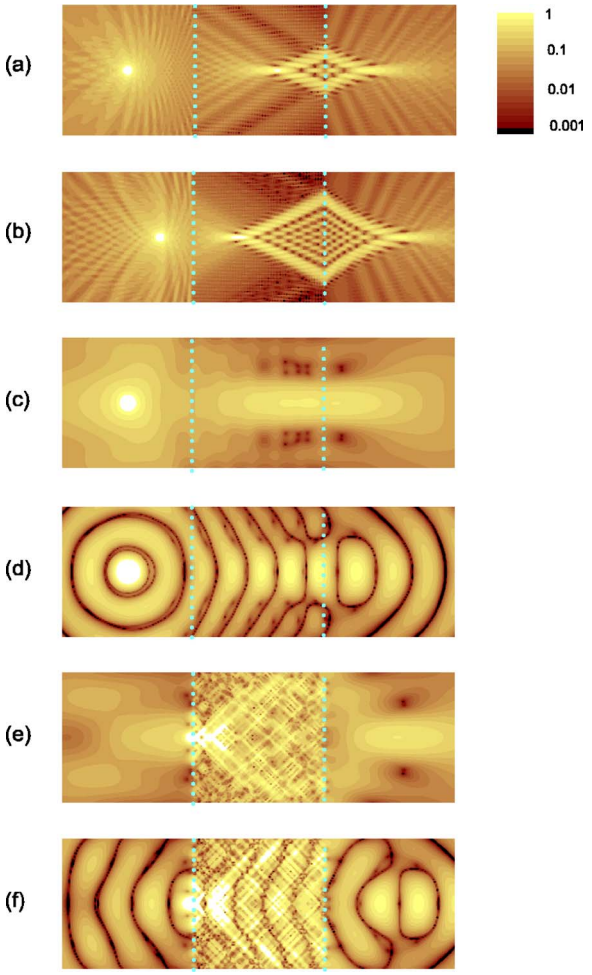

FIG. 5. (Color online) Focusing of radiation from a line source by a slab lens with $\epsilon_{xx}=1$, $\epsilon_{zz}=-1+0.0001i$. (a) Time-averaged power density when $d_1=10\lambda$, $d_2=20\lambda$. (b) Time-averaged power density when $d_1=5\lambda$, $d_2=20\lambda$. (c) Time-averaged power density when $d_1=\lambda$, $d_2=2\lambda$. (d) Instantaneous power density when $d_1=\lambda$, $d_2=2\lambda$. (e) Time-averaged power density when $d_1=0.05\lambda$, $d_2=2\lambda$. (f) Instantaneous power density when $d_1=0.05\lambda$, $d_2=2\lambda$.

tially the same as shown in Fig. 3(c), with the same caustic curves clearly visible. These types of curves have also been seen in lenses of double negative materials.[19] The distance d_1+d_3 is now equal to 17.1λ, equivalent to $0.855d_2$, and the full width at half-maximum (FWHM) at the focus is $0.7\lambda=0.035d_2$. We check that d_1+d_3 remains constant by reducing d_1 to 5λ in Fig. 5(b). Once again we find $d_1+d_3=17.1\lambda$, and the FWHM is also unchanged. In both cases, the image is considerably elongated along the z axis, having a length of 5λ.

In the geometrical optics regime $d_1, d_2 \gg \lambda$, the image size should be determined by the aberrations seen in Fig. 3(c), so a scaling down of d_1 and d_2, assuming d_1/d_2 is held constant, should lead to a corresponding scaling down of the image size. If, on the other hand, d_1 and d_2 approach wavelength dimensions, image size is determined mainly by diffraction-limiting effects. We see this by comparing Fig. 5(a) with Fig. 5(c), in which d_1 and d_2 have been reduced from 10λ and 20λ to λ and 2λ, respectively. The FWHM of the image

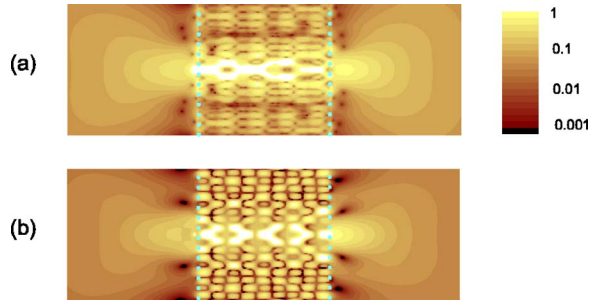

FIG. 6. (Color online) Focusing of radiation from a line source by a slab lens with $\epsilon_{xx}=1$, $\epsilon_{zz}=-5+0.000i$. The lens thickness is $d_2=2\lambda$, and the source is positioned such that $d_1=0.05\lambda$. (a) Time-averaged power density. (b) Time-averaged value of $|H_y|^2$.

changes from $0.7\lambda=0.035d_2$ to $0.46\lambda=0.23d_2$, the image now being effectively at its diffraction-limited size. In addition, the image is now closer to the lens. A snapshot of the power flow [Fig. 5(d)] helps show how focusing occurs. A plot similar to this has also been shown by Smith *et al.*[26] in an analogous s-polarization case. We check if d_1+d_3 is still independent of d_1 for this thinner slab by comparing Fig. 5(c) with Fig. 5(e), for which d_1 is reduced from λ to 0.05λ. We find that $d_1+d_3=1.18\lambda$ in both cases, and that the FWHM does not change. Figure 5(f) shows the instantaneous power flow when $d_1=0.05\lambda$, and one can clearly see how the exterior image is shifted to the right when compared with Fig. 5(d). In addition to this, careful study shows that there is an internal focus near the right-hand edge of the lens in Figs. 5(c) and 5(d) and near the left-hand edge of the lens in Figs. 5(e) and 5(f), much as geometrical optics would predict. The overall imaging behavior appears similar to that from a slab of double negative media in which the perfect lens condition $n=-1$ is not satisfied.[19,31]

Although the source is very close to the slab ($d_1 \ll \lambda$) in Figs. 5(e) and 5(f), image formation does not appear to be dictated by near-field effects. Total reconstruction of the source field, which, in double negative materials, depends on growing evanescent fields within the slab,[2] is not available to us. In our case there are no evanescent fields within the slab, as k_{2z} is real for all k_x [see Eq. (4) and Fig. 1(b)]. Evanescent fields from the source can be passed from one side of the slab to the other but, unless both the source and the image are very close to the slab ($d_1, d_3 \ll \lambda$), such fields do not appear to contribute to the image.

We can bring both the source and image close to the slab if we increase the magnitude of ϵ_{zz}. In Fig. 6 we show results for a crystal with $\epsilon_{xx}=1$ and $\epsilon_{zz}=-5+0.0001i$. d_1 and d_2 are the same as in Figs. 5(e) and 5(f). Figure 6(a) shows the time-averaged Poynting vector and Fig. 6(b) shows the time-averaged value of $|H_y|^2$. In both figures, the radiation appears to pass through the slab as a collimated beam. This type of behavior has previously been reported in photonic crystal slabs having flattened equal frequency contours at low k_x values[32] (flattening the contour is equivalent to increasing the magnitude of ϵ_{zz}).

Figure 6(a) gives the image position at $d_3=0.01\lambda$, with a FWHM of 0.36λ. The image in Fig. 6(b), on the other hand, is not separated from the slab surface, so we take $d_3=0$,

giving a FWHM value of only 0.27λ. The difference between the two figures is largely due to the evanescent waves, which do not contribute to the power flow at the image. Evanescent waves, therefore, do not take part part in the formation of the image seen in Fig. 6(a) but do contribute to the narrower image seen in Fig. 6(b)—which figure more closely represents the experimental situation is likely to depend on the exact experimental configuration.

It is worth comparing briefly the behavior of the evanescent modes in this case with the reconstruction of the evanescent components from the perfect lens discussed by Pendry.[2] In the latter case, the evanescent field grows within the slab due to surface modes. In the present case, however, there are no evanescent fields within the slab, and surface modes are not possible. Nevertheless, guided waves are allowed at certain discrete k_x values. In such cases the evanescent field decays from either side of the slab. At the relevant k_x values there are poles in the field transmitted across the slab, and these appear to contribute to the subwavelength imaging observed in Fig. 6(b). They do not, in general, lead to a simple reproduction of the source field, however, and the image does not necessarily contain a dominant central peak of the type seen in Fig. 6(b). The exact form of the image depends crucially on the values of the slab thickness and of the slab material parameters, as is the case for photonic crystals with flattened equal frequency contours,[33] and the overall behavior in the case of these higher ϵ_{zz} magnitudes appears somewhat similar to that reported for such photonic crystals.[17] Note that the poles in the transmitted field are also responsible for the instabilities, mentioned earlier, in the integral used in the transmitted field calculations, since this integral is based on a summation using a finite sampling interval. The result is that spurious features can appear in the field plot. The incorporation of a small imaginary component into ϵ_{zz} slightly smoothes out these poles, however, and this resolves the problem.

V. CRYSTAL MATERIALS SUITABLE FOR SLAB LENSES

Let us now consider how the condition $\epsilon_{xx}>0, \epsilon_{zz}<0$ can be achieved in practice. We concentrate, in this section, on natural crystals that can be used in the geometrical optics regime $d_1, d_2 \gg \lambda$. Many anisotropic crystals, such as quartz, satisfy the condition $\epsilon_{xx}>0, \epsilon_{zz}<0$ in principle, at far-infrared frequencies due to polarization dependence of certain phonon resonances.[34] If we consider these resonances as damped harmonic oscillations, we can express both ϵ_{xx} and ϵ_{zz} in the form

$$\epsilon_{uu} = \epsilon_{\infty,u} + \sum_n \frac{\rho_{n,u}\omega_{0n,u}^2}{\omega_{0n,u}^2 - \omega^2 - i\omega\gamma_{n,u}}, \tag{20}$$

where u represents either x or z. Here $\epsilon_{\infty,u}$ represents the high-frequency dielectric constant, and $\omega_{0n,u}, \rho_{n,u}$, and $\gamma_{n,u}$ represent the frequency, strength, and damping parameter, respectively, of the nth phonon mode.

Ignoring damping ($\gamma_{n,u}=0$), one can see that ϵ_{uu} becomes negative near the resonances, and since the resonant frequencies in ϵ_{zz} are not necessarily the same as those in ϵ_{xx}, the condition $\epsilon_{xx}>0, \epsilon_{zz}<0$ should be possible in suitably anisotropic materials. In practice, however, damping plays a vital role in the response, and, at thicknesses necessary for the geometrical optics experiments considered in this section, most crystals are effectively opaque near the phonon resonances. Phonon combination bands further complicate the picture. Nevertheless, if one is prepared to work at low temperatures, not only do materials with suitably low absorption exist, but they are also easy to grow in large single crystals.

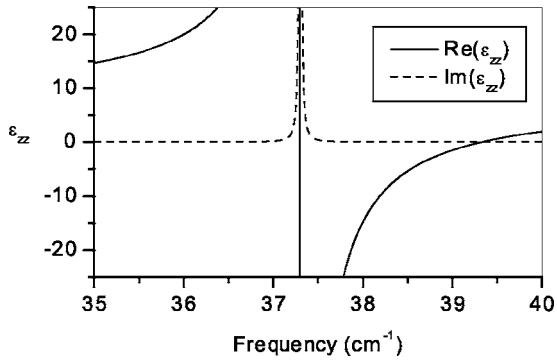

FIG. 7. Real (solid lines) and imaginary (broken lines) parts of ϵ_{zz} for TGS at 5 K.

An extremely promising material is triglycine sulfate (TGS). The crystal structure is actually biaxial, not uniaxial, but since we are only considering the case of **E** restricted to the xz plane, this makes no difference so long as x and z are both principal axes of the structure. We consider a geometry that places the crystal C_2 axis along our z axis and the crystal x axis along our own x axis. Measurements[35] at 5 K record a phonon resonance, polarized along z, at 37.3 cm^{-1} with a damping parameter of only 0.002 cm^{-1}. Using the data of Gerbaux and co-workers,[35,36] we model the resulting ϵ_{zz} in Fig. 7 (for simplicity we only model a single oscillator since there are no other close resonances). Over the given range, ϵ_{xx} can be considered constant, taking a value 3.65.[36] Figure 7 shows that the imaginary part of ϵ_{zz} is extremely small over almost the entire range, suggesting that, at low temperatures, TGS would be an excellent candidate for slab lensing experiments.

We model the focusing, by a TGS slab, of radiation from a magnetic line current source in Fig. 8. The model is the same as that used to generate Figs. 5 and 6. ϵ_{zz} is taken from Fig. 7 and $\epsilon_{xx}=3.65$, with $d_1=5$ mm and the slab thickness $d_2=10$ mm. The transmission spectrum through a slab of approximately this thickness was investigated by Hadni *et al.*,[36] who showed that it was almost totally transparent in this frequency region. As might be expected from Fig. 7, the focusing effect is highly frequency-dependent, the internal image moving further to the left and the external image moving further to the right with increasing frequency. In Fig. 8(a), at 38.73 cm^{-1}, the external and internal images roughly coincide, at the right-hand edge of the slab, having a FWHM of 0.18 mm$=0.018d_2=0.70\lambda$. Figure 8(b) shows the situation at 38.93 cm^{-1}. The internal image is now roughly at the center of the slab, with the external image to the right of it, having a FWHM of 0.21 mm$=0.021d_2=0.82\lambda$. It is interesting to compare this figure with Fig. 5(a), since they are very

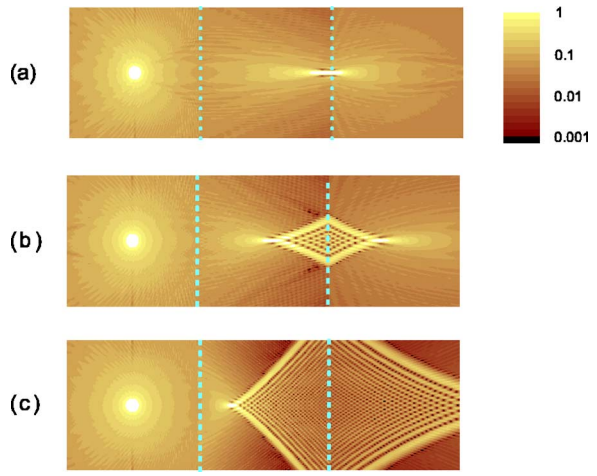

FIG. 8. (Color online) Focusing of radiation from a line source by a TGS slab of thickness 10 mm at frequency (a) 38.73 cm^{-1}, (b) 38.93 cm^{-1}, and (c) 39.13 cm^{-1}.

similar. This similarity appears to be related to the fact that, ignoring damping, $\epsilon_{zz}/\epsilon_{xx}^{1/2}$ (n_{eff} in the paraxial approximation) has the same value (−1) in both cases. In Fig. 8(c), at 39.13 cm^{-1}, the internal image has moved further to the left, and the external image now lies outside the range shown. All the trends seen in Fig. 8 are also seen in the refocusing of a normally incident *p*-polarized Gaussian beam (Fig. 9).

Negative refraction of a Gaussian beam at oblique incidence can be seen directly in Fig. 10. In modeling this figure, we consider radiation focused directly on the front surface of the slab, this time with a beam waist of 2 mm. A displacement of the emergent beam is observed, and this displacement is frequency-dependent, as can be seen by comparing Figs. 10(a)–10(c). Note that the directions of the refracted rays could equally well be calculated from Eq. (7).

VI. CONCLUSION AND DISCUSSION

From the above results it is clear that a TGS slab should display the type of lensing properties discussed by Veselago.[1]

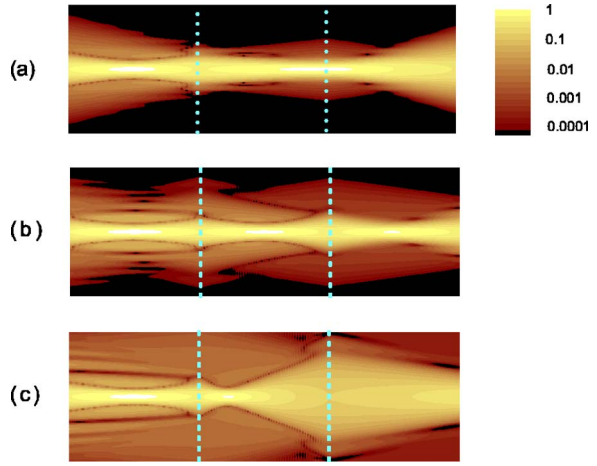

FIG. 9. (Color online) Refocusing of a normally incident Gaussian beam by a TGS slab. The parameters are d_1=5 mm, d_2=10 mm, and w=0.5 mm. (a) 38.73 cm^{-1}, (b) 38.93 cm^{-1}, (c) 39.13 cm^{-1}.

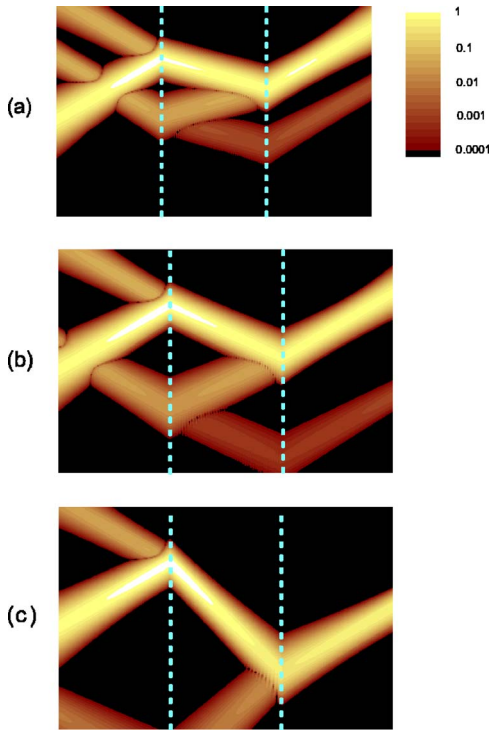

FIG. 10. (Color online) Refraction of a *p*-polarized Gaussian beam focused on the surface of a 10 mm TGS slab at θ=30°. (a) 38.73 cm^{-1}, (b) 38.93 cm^{-1}, (c) 39.13 cm^{-1}.

The frequency dependence of these properties, and of the lateral shift of a transmitted ray at oblique incidence, means that, with suitable use of stops or slits, such a slab would act as a type of narrow pass filter, and experimental investigations on this type of material appear extremely important. We have concentrated on the behavior of such a material in the geometrical optics regime since fairly simple experiments should be possible using the large crystals described. However, much thinner lenses of the type shown in Figs. 5(c)–5(f) and Fig. 6 should also be possible. Indeed, for these thinner lenses, the requirement of low absorption may be somewhat relaxed, and many other materials should be suitable.

Apart from natural crystals, it may also be useful to start considering artificial structures in which the dielectric tensor can be controlled. A simple structure applicable to far-infrared wavelengths would be a semiconductor superlattice. In the long-wavelength limit, such a structure can be considered as a uniaxial medium, and the components of the dielectric tensor can have opposing signs, as required. In fact, the discussion of negative refraction in Ref. 22 was prompted by the presence of unusual features in the experimental phonon reflectivity spectra of semiconductor superlattices.[37] However, semiconductor phonons do not usually have sufficiently low damping to allow significant transmission at thicknesses applicable to geometric optics. Nevertheless, for smaller-scale experiments, such structures may still be appropriate. For instance, Shvets[38] has noted that silicon carbide may be useful for photonic structures because it has a low loss reststrahlen region well matched to the wavelength (10.6 μm) of conventional CO_2 lasers. A superlattice incorporating this

material may therefore be a useful system to study in the context of the present work.

An alternative approach may be to consider the plasma response in a doped superlattice or multiple-quantum-well structure. If the superlattice is modulation-doped, the free carriers are separated from the donors, and very high mobilities are possible, leading to low absorption. The layer widths and doping densities are controllable, leading, in principle, to controllable dielectric tensor components. In the simplest case, a bulk-slab model, in which the superlattice components are assumed to retain their bulk properties, may be used.[39,40] In general, however, a more complete model, taking quantum confinement into account,[41] is likely to be more useful, and the conditions needed for sufficiently low absorptions require very careful consideration.

Finally, we believe that a fairly thorough analysis of the near-field effects, which appear important in situations of the type shown in Fig. 6, is called for.

ACKNOWLEDGMENTS

This work is supported by the Brazilian research agencies CNPq and CAPES.

*Corresponding author. Electronic address: thomas@uern.br
†Address for correspondence.

[1] V. G. Veselago, Sov. Phys. Usp. **10**, 509 (1968).
[2] J. B. Pendry, Phys. Rev. Lett. **85**, 3966 (2000).
[3] J. B. Pendry, A. J. Holden, D. J. Robbins, and W. J. Stewart, IEEE Trans. Microwave Theory Tech. **47**, 2075 (1999).
[4] D. R. Smith, W. J. Padilla, D. C. Vier, S. C. Nemat-Nasser, and S. Schultz, Phys. Rev. Lett. **84**, 4184 (2000).
[5] R. A. Shelby, D. R. Smith, and S. Schultz, Science **292**, 77 (2001).
[6] C. G. Parazzoli, R. B. Greegor, K. Li, B. E. C. Koltenbah, and M. Tanielian, Phys. Rev. Lett. **90**, 107401 (2003).
[7] H. Kosaka, T. Kawashima, A. Tomita, M. Notomi, T. Tamamura, T. Sato, and S. Kawakami, Phys. Rev. B **58**, R10096 (1998).
[8] M. Notomi, Phys. Rev. B **62**, 10696 (2000).
[9] C. Luo, S. G. Johnson, J. D. Joannopoulos, and J. B. Pendry, Phys. Rev. B **65**, 201104(R) (2002).
[10] C. Luo, S. G. Johnson, and J. D. Joannopoulos, Appl. Phys. Lett. **81**, 2352 (2002).
[11] C. Luo, S. G. Johnson, J. D. Joannopoulos, and J. B. Pendry, Phys. Rev. B **68**, 045115 (2003).
[12] E. Cubukcu, K. Aydin, E. Ozbay, S. Foteinopoulou, and C. M. Soukoulis, Nature **423**, 604 (2003).
[13] X. Wang, Z. F. Ren, and K. Kempa, Opt. Express **12**, 2919 (2004).
[14] S. Xiao, M. Qiu, Z. Ruan, and S. He, Opt. Express **11**, 746 (2003).
[15] S. Foteinopoulou and C. M. Soukoulis, Phys. Rev. B **67**, 235107 (2003).
[16] P. V. Parimi, W. T. Lu, P. Vodo, and S. Sridhar, Nature **426**, 404 (2003).
[17] E. Cubukcu, K. Aydin, E. Ozbay, S. Foteinopoulou, and C. M. Soukoulis, Phys. Rev. Lett. **91**, 207401 (2003).
[18] A. Berrier, M. Mulot, M. Swillo, M. Qiu, L. Thylén, A. Talneau, and S. Anand, Phys. Rev. Lett. **93**, 073902 (2004).
[19] J. B. Brock, A. A. Houck, and I. L. Chuang, Appl. Phys. Lett. **85**, 2472 (2004).
[20] Z. Ye, Phys. Rev. B **67**, 193106 (2003).
[21] D. R. Smith, D. Schurig, M. Rosenbluth, S. Schultz, S. A. Ramakrishna, and J. B. Pendry, Appl. Phys. Lett. **82**, 1506 (2003).
[22] T. Dumelow and D. R. Tilley, J. Opt. Soc. Am. A **10**, 633 (1993).
[23] P. A. Belov, Microwave Opt. Technol. Lett. **37**, 259 (2003).
[24] J. A. Kong, *Electromagnetic Wave Theory* (Wiley Interscience, 1990).
[25] D. R. Smith and D. Schurig, Phys. Rev. Lett. **90**, 077405 (2003).
[26] D. R. Smith, P. Kolinko, and D. Schurig, J. Opt. Soc. Am. B **21**, 1032 (2004).
[27] X. Hu and C. T. Chan, Appl. Phys. Lett. **85**, 1520 (2004).
[28] J. A. Kong, B.-I. Wu, and Y. Zhang, Appl. Phys. Lett. **80**, 2084 (2002).
[29] E. Hecht, *Optics*, 2nd ed. (Addison-Wesley, Reading, MA, 1974).
[30] J. R. Wait, *Electromagnetic Waves in Stratified Media*, Vol. 3 of International Series of Monographs on Electromagnetic Waves (Pergamon Press, New York, 1962).
[31] P. F. Loschialpo, D. W. Forester, D. L. Smith, F. J. Rachford, and C. Monzon, Phys. Rev. E **70**, 036605 (2004).
[32] Z.-Y. Li and L.-L. Lin, Phys. Rev. B **68**, 245110 (2003).
[33] C. Luo, S. G. Johnson, J. D. Joannopoulos, and J. B. Pendry, Opt. Express **11**, 746 (2003).
[34] W. G. Spitzer and D. A. Kleinman, Phys. Rev. **121**, 1324 (1961).
[35] X. Gerbaux, M. Tazawa, and A. Hadni, Ferroelectrics **215**, 47 (1998).
[36] A. Hadni and X. Gerbaux, Ferroelectrics **248**, 15 (2000).
[37] T. Dumelow, T. J. Parker, S. R. P. Smith, and D. R. Tilley, Surf. Sci. Rep. **17**, 151 (1993).
[38] G. Shvets, Phys. Rev. B **67**, 035109 (2003).
[39] N. Raj and D. R. Tilley, Solid State Commun. **55**, 373 (1985).
[40] V. M. Agranovich and V. E. Kravstov, Solid State Commun. **55**, 85 (1985).
[41] A. C. Tselis and J. J. Quinn, Phys. Rev. B **29**, 3318 (1984).